Pd and GDC Co-infiltrated LSCM Cathode for High-temperature CO_2 Electrolysis using Solid Oxide Electrolysis Cells

Seokhee Lee[1]*, Sung Hun Woo*[1]*, Tae Ho Shin*[1*] *and John T. S. Irvine*[2]

[1]Energy and Environmental Division, Korea Institute of Ceramic Engineering and Technology, Jinju-si, Gyeongsangnam-do 52851, Republic of Korea

[2]School of Chemistry, University of St Andrews, KY16 9ST, Fife, Scotland, UK

*Corresponding Author

Dr. Tae Ho Shin

Energy Materials Center

Korea Institute of Ceramic Engineering & Technology, 52851, Republic of Korea

Tel: +82-055-792-2585 and Fax: +82-055-792-2469

E-mail: ths@kicet.re.kr, ceramist95@gmail.com

Abstract

The electrochemical reduction of CO_2 using a highly efficient solid oxide electrolyzer could be considered an alternative to the advanced utilization of CO_2. The La(Sr)Cr(Mn)O_3 (LSCM) perovskite oxide has previously been examined as a promising ceramic cathode material for application in a CO_2 solid oxide electrolyzer at high temperatures. However, LSCM suffers from low electrocatalytic activity towards CO_2 reduction. In this study, a modified LSCM-based cathode material is fabricated by co-infiltrating Pd metal and $Ce_{0.8}Gd_{0.2}O_{1.9}$ (GDC) nanoparticles on the surface of the LSCM scaffold. Structural characterization and electrochemical analysis of the high-temperature CO_2 electrolysis procedure are conducted for various CO/CO_2 mixtures and at different operating temperatures. The enhanced electrocatalytic activity of the Pd-GDC co-infiltrated LSCM cathode compared to LSCM is attributed to the increased numbers of active triple phase boundaries and surface oxygen vacancies resulting from the co-infiltration of Pd-GDC nanoparticles on the LSCM cathode.

Keywords: Solid Oxide Electrolysis Cells, $(La_{0.75}Sr_{0.25})_{0.97}Cr_{0.5}Mn_{0.5}O_3$, $Ce_{0.8}Gd_{0.2}O_{1.9}$, nanocatalysts, Co-Infiltration

1. Introduction

The emission of CO_2 remains a significant environmental challenge in the 21st century due to its formation from the widely employed fossil fuels and its association with global warming. As one means to address this issue, alternative energy sources can be employed, whereby several innovative systems have been investigated for energy conversion and storage from electrochemical reactions, with examples including solid-state batteries, redox flow batteries, and fuel cells (e.g., solid oxide fuel cells, SOFCs). However, further innovative research is required to deliver high efficiency next-generation electrochemical devices with high performances, low CO_2 emissions, and high efficiencies. To address these points, not only CO_2 reduction and storage systems, but also alternative energy conversion and storage systems are required, whereby these systems should exhibit high efficiencies and employ environment-friendly technologies. Thus, solid oxide electrolysis cells (SOECs) have recently attracted considerable interest as highly efficient electrolyzers. More specifically, SOECs have been mainly employed in hydrogen electrolysis and in the highly efficient co-electrolysis of CO_2/H_2O to yield syngas (H_2/CO) using renewable electrical energy sources [1-5].

Generally, SOECs require a high operating temperature (>973 K) to reduce the ohmic resistance of the electrolyte because of the favorable thermodynamics and kinetics of the electrocatalytic CO_2 reduction process at high temperatures [6, 7]. Thus, the corresponding electrode materials must be exhibit sufficient stability and good catalytic properties over a wide temperature range and must be tolerant of carbon coking. Commonly, SOECs employ Ni-based cermets that exhibit high electrocatalytic activities as cathode materials [8-10]. However, these cermets are not suitable for high-temperature CO_2 electrolysis due to the fact that the fuel composition must be strictly controlled to maintain a metallic catalyst and to avoid carbon deposition [11-13]. Thus, $La(Sr)Cr(Mn)O_3$ (LSCM) has been recently considered as a promising cathode material for high-temperature CO_2 electrolysis due to its high redox stability and acceptable conductivity under the reducing conditions [14, 15]. However, the electrochemical performance of the ceramic electrode remains low compared to that obtained using a Ni cermet electrode, in particular, due to a poor CO_2 electrocatalytic activity on the electrode surface. As a result, the modification of LSCM cathodes has received growing attention with the purpose of improving their performance [16,17].

In the CO_2 electrolysis process, the CO_2 adsorption step on the surface of the cathode material plays a particularly important role [18]. The introduction of nanoparticles onto the LSCM cathode materials would therefore be expected to enhance the CO_2 adsorption ability and electrocatalytic activity of the cathode, thereby enhancing their performance in the electrolysis of CO_2 over SOECs. Although wet infiltration is a frequently used to achieve high electrode activities in SOECs [19], cathode materials prepared by this means for application in the CO_2 electrolysis process gave poor results [20].

In a previous study, an LSCM-based electrode infiltrated with V_2O_5 and Ni was investigated for CO_2 and steam electrolysis; however, the electrode exhibited a poor durability [21]. Cu was also used to provide electronic conductivity and catalytic activity in the CO_2 electrolysis process, yet the system suffered from increased resistance upon increasing the CO_2 feed, and stability was also issue due to the low melting temperature of Cu [22, 23]. The use of infiltrated Pd as a nanocatalyst in environmental catalysis was also considered promising for the modification of LSCM cathode materials. Indeed, the infiltration of 0.5 wt% Pd, 5 wt% $Ce_{0.48}Zr_{0.48}Y_{0.04}O_2$, and 45 wt% LSCM into a YSZ scaffold resulted in the formation of a superior fuel cell electrode compared with the Ni-YZS cermet. However, neither the performance of this material in the electrolyzer mode nor the stability of the system in a CO-CO_2 mixture were examined [20].

Thus, in this study, the preparation of a Pd-GDC@LSCM cathode via the infiltration process is reported with the aim of enhancing the cathode performance in the CO_2 dissociation step of SOECs. In addition, the microstructure and performance of the infiltrated-derived cathode are characterized to disclose the role of the Pd-GDC ($Ce_{0.8}Gd_{0.2}O_{1.9}$) nanoparticles in the CO_2 electrolysis process, and the mechanism of the electrocatalytic activity enhancement is discussed.

2. Experimental

For the electrolyzer test, Pd-GDC@LSCM|YSZ|LSCF unit cells were fabricated. YSZ electrolyte supports were prepared via the tape casting method and were fired at 1773 K. The diameter of the obtained pellets was 20 mm, and their thickness was 350 µm. Pore former (Glassy Graphite/Graphite flak 50/50 by weight) and YSZ powder were mixed to form the porous YSZ layer. Porous YSZ Ink was then screen-printed on one side of the YSZ electrolyte and sintered at 1473–1623 K. The LSCM/YSZ (50/50 by weight) composite was also screen-printed and sintered at 1373 K for 1h. To form Pd-GDC@LSCM cathode layer on the YSZ electrolyte support, CGO($Ce(NO_3)_3.6H_2O/Gd(NO_3)_3.6H_2O$ 90/10 by weight) and Pd were infiltrated into the cathode surface and sintered at 973 K. The counter electrode and reference electrode were LSCF and LSCF/YSZ (50/50 by weight), which were screen-printed on the opposed side of the YSZ electrolyte, and fired at 1373 K. The area of the circular working electrode was 1.13 cm^2, while the area of the counter electrode was 1.03 cm^2. The electrodes ranged in thickness from 30 to 40 µm.

The cell was placed between two alumina tubes and sealed in the cathode chamber using ceramic cement (Aremco), and the resulting assembly was placed in a temperature-controlled furnace. Pt probes were employed to collect the current, and an R-type thermocouple was placed close to the cell to monitor the cell operating temperature. The furnace was heated to 1173 K for electrochemical evaluation, and when the desired temperature was reached, humidified H_2/Ar was allowed to flow into the cathode side to evaluate the open-circuit voltage and to check that the cell was sealed. Following tests in a H_2/steam atmosphere, the H_2 flow was slowly reduced to zero, while the CO_2/CO gas mixture (30 mL min^{-1} total flow rate) was introduced at the fuel side (i.e., the SOEC cathode side), and air (100 mL min^{-1} constant flow rate) was flushed through the anode side. The cell performance was characterized in atmospheres containing different CO_2/CO volume ratios, namely 50/50 and 30/70. The single-cell electrochemical test involved DC polarization testing and AC impedance measurements. More specifically, for the DC polarization testing, I-V curves were recorded in both the electrolysis and fuel cell manners by varying the current. AC impedance measurements were conducted using a Solartron Electrochemical Workstation. Impedance spectra, with an AC voltage amplitude of 10 mV and a frequency ranging from 105 Hz to 0.1 or 0.015 Hz, were recorded under OCV conditions and under the application of different voltages to the cell, which could give more meaningful results, due to the fact that SOECs involve active rather than passive processes. In order to distinguish anodic impedance from total impedance spectra, Pt reference wire, which was attached to the surface of the anode electrode spaced appropriately from anode, was employed (Figure S4(e)). In addition, we performed off-line GC analysis to clarify gas-phase CO_2 electrolysis to CO and CO_2 which are available for cathode electrocatalytic reduction reaction. The measurements of electrocatalytic CO_2 reduction at constant voltages were conducted at 1123 K and the CO product and CO_2 remaining were detected by Gas chromatography(GC, 6790N (G1530N), USA) equipped with a molecular sieve column and TCD detector.

3. Results and Discussion

The infiltration process involves the steps to synthesize the Pd-GDC@LSCM electrode illuminated in Figure 1(a). The porous electrode backbone is prepared and then the backbone is fired at high temperature to ensure excellent bonding with the electrolyte, excellent connectivity for effective conduction of electron and oxygen ion, and good structural stability of the electrode under operation conditions. A liquid solution containing the stoichiometric metal salt precursors for Pd-GDC is introduced into a pre-sintered backbone of LSCM. After subsequent thermal treatment, Pd-GDC nanoparticles are formed on the surface of the backbone of LSCM (Pd-GDC@LSCM). A schematic representation of the SOEC cell fabricated using the Pd-GDC@LSCM cathode and a LSCF-YSZ anode is shown in Figure 1(b). During CO_2 electrolysis in SOECs at high temperatures, CO_2 molecules initially adsorb on the surface of the lattice oxygen species adjacent to the oxygen vacancies to form carbonate intermediates. These carbonate intermediates accept electrons and subsequently dissociate into CO and O^{2-} at the triple phase boundary (TPBs). Finally, CO desorbs from the surface while O^{2-} is incorporated into the oxygen vacancies and moves to the electrolyte. The proposed mechanism suggests that the performance of the SOEC cathodes is determined by two factors, namely the intrinsic electrocatalytic activity of the TPBs, and the chemical adsorption of CO_2 on the surface of the cathode materials [24-26]. Thus, as indicated by the cathode structure, Pd-GDC nanoparticles are decorated on the LSCM and the confined interface architecture. This nano-structured Pd+GDC@LSCM can lead to enhanced electrocatalytic activities and coking resistance due to the metal/oxide interface interactions. As shown in Figure S1(a) and (d), it was confirmed that nano Pd particles and Gd doped Ceria were distributed on LSCM surface through SEM images and EDS mapping analysis. Accordingly, the presence of PdO particles on the cathode surface after infiltration process could be also investigated by XRD analsysis as shown in Figure S2.

Figure 2 shows the SEM images of the LSCF-YSZ anode and the Pd-GDC@LSCM cathode, whereby the YSZ electrolyte appears as a compact layer after firing at 1773 K, and this allows it to transfer oxygen ions from the cathode to the anode during CO_2 electrolysis [27]. In addition, the porous Pd-GDC@LSCM and LSCF-YSZ electrodes with a thickness of ~40 μm are closely attached to the YSZ electrolyte. An HR-SEM image of the Pd-GDC@LSCM cathode is shown in Figure 2 (c) and (d), where it can be seen that the infiltrated Pd-GDC nanoparticles are highly dispersed on the LSCM surface. These nanoparticles are believed to be ideal for the expanding surface area to promote the cathode reaction; Pd and nano-structured ceria based additives are well known for giving a high catalytic effect [28, 29, 52]. Accordingly, not only the CO_2 electrolysis performance but also hydrogen fuel cell electrode reactivity of the Pd-GDC co-infiltrate LSCM cathode was higher, compared with that of LSCM as shown in Figure S3(a). Sequentially, the activation energy related to the polarization reaction on the electrode surface during CO_2 electrolysis could be dramatically decreased by Pd-GDC co-infiltration, compared with GDC infiltrated one and genuine LSCM cathode (Figure S3(b)). It was therefore expected that the infiltration-derived cathode could provide extended TPBs and enhance the electrochemical activity of the cathode. Overall, the wet infiltration process imparts a greater flexibility to optimize the SOEC electrode microstructure, since the electrode materials can be fired at different temperatures to tune their properties according to their functions. In addition, the infiltration process increases the number of Pd-GDC active sites for the reaction, in addition to ensuring a uniform distribution on the cathode surface.

The electrochemical performance of SOFC was initially estimated prior to the SOEC mode operation of the CO_2 reduction electrolysis process. Figure 3 shows the current-terminal voltage (I-V) and current-power density (I-P) curves of the cell containing the Pd-GDC@LSCM electrode under the SOFC operation mode, in the case where humidified pure hydrogen was employed as a fuel. Despite the thick electrolyte layer (~350 μm as shown in the cell configuration, Figure 2(b)), the maximum power density reached reasonable values of ~220 and 170 mW cm^{-2} at 1123 and 1073 K, respectively. As shown in Figure 3(b), the impedance spectrum mainly consists of more than two semicircles, which were attributed to the activation, the various reactions taking place on the modified surface, and the diffusion overpotential of the system.

Subsequently, to evaluate its electrochemical performance in the CO_2 reduction electrolysis reaction, the single unit cell containing the Pd-GDC@LSCM electrode was tested using a CO_2-CO mixture at increasing temperatures. Thus, Figures 4(a) and 4(b) show the temperature-dependent I-V curves for CO_2 electrolysis between 1023 and 1123 K under the following gas feed conditions: a mixture of 50%CO_2/50%CO and 70%CO_2/30%CO on the cathode side with a flow rate of 100 mL min^{-1}. A fairly linear relationship between the potential and current density can be seen in Figure 4(a), only a marginal reduction in performance was observed for the cell operated in the CO_2-CO mixture (50:50 vol.%). Under an identical voltage of 1.5 V, the CO_2 electrolysis current densities were found to be 364, 297, and 256 mA cm^{-2} at 1123, 1073, and 1023 K, respectively, which indicates that the electrochemical performance for CO_2 electrolysis is slightly temperature-dependent in the case of the CO_2-CO mixture (50:50 vol.%). The current density of 364 mA cm^{-2} is higher than almost all of the reports from 25 to 278 mA cm^{-2}, for electrolyzing CO_2/CO mixture at 1073 and 1123 K using various electrode materials as shown in Table 1. On the other hand, the electrical performance appeared to be generally independent of the temperature, although a similar phenomenon was observed in the case of the 30 vol.% CO_2 mixture, as shown in Figure 4(b). More specifically, the open-circuit voltages

(OCV) of the Pd-GDC@LSCM cathode operating in CO_2-CO mixtures (50:50 and 70:30 vol.%) are displayed along with the working temperatures employed, and it was found that the obtained value was similar to the theoretical values (0.94 V and 0.98 V under CO_2-CO mixtures of 50:50 and 70:30 at 1073 K, respectively) expected from the Nernst equation [36, 37]. This result was attributed to the gas sealing effect in Pd-GDC@LSCM electrode-based cell. In addition, the impedance responses of the Pd-GDC@LSCM cathode operated in the CO_2-CO mixtures at 1023 K are compared in Figures 4(c) and 4(d). In this case, the intercept of the impedance arc with the real axis in the high-frequency regime represents the ohmic resistance R_s, with contributions mainly from the YSZ electrolyte, whereas the intercept of the impedance arc with the real axis in the low-frequency region represents the total electrode resistance, with the difference between these two intercepts being the polarization resistance, R_p. As shown in Figures 4(c) and 4(d), R_s remains constant upon increasing the operating voltage from the OCV. However, R_p decreases upon increasing the voltage from 0.2 to 0.5 V, indicating faster electrolysis reaction kinetics at a higher working potential. In addition, the variation in the low-frequency arc at different operation potentials suggests that the dissociative adsorption of active species on the electrode surface and/or surface diffusion of adsorbed species for CO_2 reduction processes may play a vital role in the CO_2 reduction process on Pd-GDC@LSCM. The impedance responses of the Pd-GDC@LSCM cathode in the presence of different gas compositions also indicated that R_s does not vary with the gas composition, although R_p reduces with a decreasing CO_2/CO ratio, thereby suggesting that the higher concentration of CO_2 present in fuels retards the CO_2 dissociation process, and in particular, the surface reaction processes [38, 39]. Upon variation in the CO_2/CO ratio or CO_2 electrolysis at higher loads, the CO content increases, and the retarding effect of the CO_2 gas is mitigated, thereby resulting in a reduction in R_p. These results may therefore contribute to the higher CO_2 electrolysis performance at lower CO_2/CO ratios, and upon the application of higher voltages to the Pd-GDC@LSCM cathode.

As shown in Figure 5, the electrochemical performances for the SOEC and SOFC modes were symmetrically fitted using a Tafel plot for the anodic and cathodic branches using the Butler-Volmer type equation [40]:

$$\boldsymbol{i = i_o\, nF \left[C_f^s\, exp \left[\frac{\beta_{cat} nF\Delta E(\eta_{cathodic})}{RT} \right] - C_r^s\, exp \left[-\frac{\alpha_{an} nF\Delta E(\eta_{anodic})}{RT} \right] \right]} \tag{1}$$

where $\boldsymbol{i}$ **and** $\boldsymbol{i_o}$ are the current and exchange current density, $\boldsymbol{C_f^s}$ **and** $\boldsymbol{C_r^s}$ are the forward and backward reaction constants related to the concentration on the surface, F, R, and T have their usual chemical meanings, $\boldsymbol{\eta}$ is the overpotential, and $\boldsymbol{\alpha_{an}}$ **and** $\boldsymbol{\beta_{cat}}$ are the symmetry factor and charge transfer coefficient for the anodic and cathodic reactions, respectively. The transfer coefficients, $\boldsymbol{\alpha_{an}}$ and $\boldsymbol{\beta_{cat}}$ (*1-α*) were calculated as determined by the Tafel slopes of the cathodic and anodic branches given by the following relationship [41]:

$$\boldsymbol{a + b \log i} \tag{2}$$

$$\boldsymbol{b_{c\ or\ a} = \frac{2.303\, RT}{-\alpha_{an}(\text{or}\ \beta_{cat})\, nF}} \tag{3}$$

In the high current ranges, plot fitting exhibited a high linearity, thereby indicating that the Tafel behavior and that slope are symmetric due to their similar anodic and cathodic transfer coefficients. However, an asymmetric SOEC/SOFC reaction may also be possible due to the lower overall charge transfer coefficients (α_an + β_cat < 1) than the normal value of 1. In our case, the calculated transfer coefficient was less than 0.5, it might be implicated in solid electrolyte, which is not highly conductive and insufficient symmetric reverse reaction because of the conduction behavior of solid electrolyte much dependant on temperature than whilst non-liquid electrolyte. Thus, this part will continue to need further detailed studies of the SOEC case later. In any case, this could be accounted for by considering the complicated polarization reaction steps taking place on the surface during CO/CO_2 adsorption and the subsequent redox reaction. Reversible SOEC/SOFC charge transfer reaction does in fact complicate the gas reaction on the electrode surface at high temperatures, and so the comparable charge coefficients may not be predicted by the simple Butler-Volmer equation model. To examine this in further detail, additional experimental investigations must be carried out and considered. In particular, the high-temperature CO_2 electrolysis process involving several ambiguous catalytic gas reactions on the electrode surface will be further examined in our future works. However, as shown in Figure 5, the logarithm current of the Pd-GDC@LSCM cathode in the SOEC mode is slightly higher than that of the SOFC mode for the CO_2/CO gas mixture. It is possible that this superior catalytic performance is related to the CO_2/CO surface chemisorption reduction reaction taking place in the SOEC process, due to the presence of the infiltration-derived Pd-GDC@LSCM electrode [42].

Based on the above results, the area-specific resistance was obtained from equivalent-circuit analysis using the electrochemical impedance spectra (EIS) of the Pd-GDC@LSCM cathode at different temperatures and voltages (OCV and 0.5 V) in a CO_2/CO (50:50 vol.%) atmosphere, as shown in Figure 6(a). A summary of the equivalent-circuit analysis from the EIS of the Pd-GDC@LSCM cathode is displayed in Table 2, where it can be seen that the calculated results correspond well with the simulated results, indicating the reliability of the employed equivalent circuit. Upon reducing the temperature, R_s and R_p increase significantly, resulting in a marked decline in the performance of the Pd-GDC@LSCM cathode. It is clear that the high-frequency arc (R_{p1}) increases only at a small magnitude as the temperature decreases (i.e., from 0.155 Ω cm^2 at 1123 K and 0.289 Ω cm^2 at 1023 K), while the low-frequency arc (R_{p2}) significantly increases with decreasing temperature up to 1.359 Ω cm^2 at 1023 K (i.e., double the value obtained at 1073 K). At a potential of 0.5 V, R_{p1} and R_{p1} display similar trends to those obtained at the OCV, however, the values are lower, indicating that the cathode kinetics are fast due to the increasing working potential. The low-frequency arc is likely related to the dissociative adsorption of the active species on the cathode surface, and to surface diffusion of the adsorbed species for the CO_2 reduction processes [43]. The above results therefore indicate that the low-frequency arc related to the surface adsorption/desorption equilibrium and surface diffusion plays a considerable role in the overall CO_2 electrolysis process compared to the high-frequency arc, which is related to the charge transfer processes. As a result, the surface activity becomes the rate-determining step for CO_2 electrolysis as the operating temperature drops.

To compare the performance of the GDC-LSCM composites fabricated via different processes, the R_p (R_{p1} + R_{p2}) values of the various conditions are summarized in Table 3. As indicated, the R_p value of Pd-GDC@LSCM was smaller than those of the GDC-LSCM composites, thereby indicating that the infiltration process results in a decreased R_p. This can be accounted for by considering that the modified microstructure containing the highly dispersed Pd-GDC nanoparticles on the LSCM surface increases the number of active reaction sites and cathode TPBs, thereby enhancing the cathode electrochemical properties. In addition, the electronic conductivity of LSCM is due to the fact that it is a p-type conductor, and so the addition of an oxygen ion-conducting phase such as GDC would significantly promote the ionic conductivity and enhance the cathode performance. Generally, Gd doping and nano-sized ceria are well known for benefit from the presence of oxygen vacancy defects due to the insertion of rare-earth ions into the CeO_2 lattice [44-47]. This could then be confirmed by the overall CO_2 electrochemical reduction process presented in Eq. (4), where $V_{\ddot{O}}$, e^-, and O_o^x represent an oxygen vacancy provided by GDC, a free-electron from the cathode [48].

$$CO_2 + V_{\ddot{O},GDC} + 2e^- \text{->} CO + O_O{}^{X}{}_{,GDC} \qquad (4)$$

In the GDC-LSCM composite cathode, the CO_2 electrochemical reduction process could be executed through Equation 4, where $V_{\ddot{O},GDC}$ and $O_O{}^X{}_{,GDC}$ indicate oxygen vacancies. The active reaction area for CO_2 reduction is extended by adding the highly oxygen ion-conducting phase to GDC. The promoting oxygen vacancy defects of nano-sized GDC distributed on the LSCM cathode via infiltration were accordingly confirmed by Raman spectra as shown in Figure 7. Comparing with only ceria Raman shift band (458 cm^{-1}) of commercial GDC powder (FCM Co. Ltd. USA), it clearly shows that the peaks between 540 and 600 cm^{-1}, which related to intrinsic oxygen vacancy, exist in Raman shift of nano-sized Gd doped CeO_2, synthesized at 1173 K from metal nitrate solution for infiltration drop, as shown in below Figure 7(a). Furthermore, to confirm the enhancing cathodic performance during CO_2 reduction through oxygen vacancies of infiltrated GDC on LSCM cathode, Raman spectra of GDC infiltrated LSCM cathode and Pd-GDC co-infiltrated LSCM cathode, were investigated as shown in Figure 7(b). GDC infiltrated cathode and Pd-GDC co-infiltrated cathode samples show two weak oxygen vacancy bands at between ca. 540 and 600 cm^{-1}. This suggests that the Gd doping of ceria with nano-structure different Gd cations and nano-lattice might induce a different type of oxygen vacancy and it is a similar tendency to other previous works [49, 50]. In addition, the formation of Pd is likely promoted by the presence of CO_2, which results in the enhanced catalytic properties observed for the cathode in the CO_2 electrolysis process. As a result, the Pd-GDC co-infiltrated LSCM material can be considered a promising alternative cathode material for application in the high-temperature CO_2 electrolysis process. It should also be noted here that the overpotential is an important factor in terms of evaluating the electrochemical properties of the electrode; it is well known that a lower overpotential implies a higher electrocatalytic activity. Thus, Figure 6(b) shows the overpotential values of the Pd-GDC@LSCM cathode at a working temperature of 1123 K under a CO_2/CO (50:50 vol.%) atmosphere. The concentration and activation overpotential values are 115.05 and 53.16 mV at a current density of 300 A cm^{-2} (loading potential = 0.5 V), respectively. In the Pd-GDC@LSCM cathode, the activation overpotential at R_{p1} is smaller than that of the concentration overpotential at R_{p1}. This decrease in the activation overpotential in the Pd-GDC@LSCM cathode can be demonstrated in the modified microstructure containing the highly dispersed co-infiltrated surface Pd-GDC nanoparticles due to the increased number of active reaction sites, which extend the cathode TPBs. The observation of a low overpotential value indicated once again that the Pd-GDC@LSCM cathode is an attractive candidate for use in high-temperature CO_2 electrolysis.

Figure 8 shows the cathode resistance obtained for the Pd-GDC@LSCM electrode as a function of the reciprocal temperature, i.e., the Arrhenius plots at the OCV and at 0.5 V under a CO_2/CO (50:50 vol.%) atmosphere. As indicated, the Arrhenius plots exhibit a good linearity over the whole operating temperature range, and the linear fit gives an activation energy of ~49.2 kJ mol^{-1} for the area-specific resistance (ASR, $R_s + R_p$) at the OCV, which is significantly higher than that obtained at 0.5 V (i.e., 24.77 kJ mol^{-1}), thereby demonstrating faster cathode kinetics at the higher working potential. In addition, the Arrhenius plots give activation energies of approximately 68.93, 62.99, and 70.52 kJ mol^{-1} for R_p, R_{p1}, and R_{p2}, respectively, while at a working potential of 0.5 V, the Arrhenius plots give activation energies of approximately 35.43, 44.51, and 31.36 kJ mol^{-1} for R_p, R_{p1}, and R_{p2}, respectively. It therefore appears that the activation energy of R_{p2} is responsible for the high activation energy of R_p, which confirms that the low-frequency arc related to the surface kinetics plays a dominant limiting role for CO_2 electrolysis on the Pd-GDC@LSGM cathode. Moreover, the activation energy values calculated for our system were found to be significantly smaller than those of the pure GDC and GDC-LSCM materials fabricated by screen-printing under a similar atmosphere [51]. These results can be explained by considering the contributions from the modified LSCM microstructure containing the highly disperse surface Pd-GDC nanoparticles.

Figure 9 shows the CO production yield and CO_2 formation rate (i.e., the difference between the CO_2 and CO formation rates) from the electrocatalytic reaction of the Pd-GDC@LSCM electrode at 1123 K under a CO_2/CO (50:50 vol.%) atmosphere. According to Figure 9(a), stable current constant of 125, 280, 600, 913 mA cm^{-2} could be obtained by 1.091 1.391, 1.691, and 1.891 V, respectively. The theoretical formation rate of CO from Faraday's law is plotted as a dashed line. As indicated, the CO formation rate increased gradually upon increasing the current density, i.e., a higher applied potential, and the observed CO formation rate corresponded closely with Faraday's law. In contrast, the CO_2 formation rate was found to decrease upon reducing the current density. Moreover, the slopes of the CO_2 and CO formation rates, which follow Faraday's law, are almost identical, thereby implying that the CO_2 conversion rate corresponds with the CO formation rate. In any case, the cell of Pd-GDC@LSCM/YSZ/LSCF exhibits Faradaic efficiency of over 90% for electrocatalytic CO_2 electrolysis as shown in Figure 9(b). It may suggest that almost no carbon coke during CO_2 electrocatalytic electrolysis on the Pd-GDC@LSCM cathode. In CO_2 electrolysis, CO is the main product, and its formation dominates on Pd-GDC@LSCM. Furthermore, the stable voltage behavior of the Pd-GDC co-infiltrated LSCM cathode was verified for over 100 h on the practical CO_2 electrolysis operating condition, at 1073 K and 100% CO_2 gas feeding in the galvanostatic mode at the applied constant current density of 100 ~200 mA cm^{-2} (Figure S4(a)). Therefore, under the CO_2 electrolysis conditions employed herein, our Pd-GDC co-impregnated LSCM material can be regarded as a promising cathode material for application in high-temperature CO_2 electrolysis.

4. Conclusions

In conclusion, we successfully developed a modified La(Sr)Cr(Mn)O_3 (LSCM) perovskite oxide microstructure containing highly disperse surface Pd metal and $Ce_{0.8}Gd_{0.2}O_{1.9}$ nanoparticles (i.e., Pd-GDC@LSCM) for application as a cathode in the high-temperature CO_2 electrolysis process. This material was synthesized by the co-infiltration of Pd-GDC on the LSCM surface. The obtained Pd-GDC@LSCM materials presented micro-sized pores and highly dispersed Pd-GDC nanoparticles, which interacted with the LSCM particles to allow the effective gas penetration of CO_2 and CO, and extend the triple phase boundaries to enhance the electrochemical activity. The electrochemical performance of the infiltration-derived Pd-GDC on the surface of the LSCM cathode was found to vary depending on the operating voltage and CO_2/CO ratio employed. Although no significant variations in R_s were observed, R_p decreased upon increasing the voltage and CO concentration due to the accelerated cathode kinetics. The activation energy for the area-specific resistance of the Pd-GDC@LSCM cathode was found to be 49.2 kJ mol^{-1} at the open circuit voltage and 24.77 kJ mol^{-1} at 0.5 V. These values are significantly smaller than those reported in the literature for a similar CO_2-CO ratio. In addition, using our system, CO_2 was reduced at a rate of 2362 µmol cm^{-2} min^{-1} at 1123 K and 0.5 V, and the CO_2 conversion rate was comparable to the formation rate of CO. These preliminary results indicate that the introduction of Pd-GDC onto the surface of an LSCM cathode via infiltration gives a promising cathode material for use in high-temperature CO_2 electrolysis applications.

Acknowledgements

This work was supported by the Technology Innovation Program (grant no. 20182010600400) funded by the Ministry or Trade, Industry & Energy (MI, Korea). Support was also provided by the Technology Innovation Program (Grant Nos. 20004963) funded by Ministry of Trade, Industry and Energy (MOTIE) of Korea.

References

[1] J.T.S Irvine, D. Neagu, M.C. Verbraeken, C. Chatzichristodoulou, C. Graves, M.B. Mogensen, Evolution of the electrochemical interface in high-temperature fuel cells and electrolysers, Nat. Energy 1 (2016) 15014. https://doi.org/10.1038/nenergy.2015.14.

[2] Y. Zheng, J. Wang, B. Yu, W. Zhang, J. Chen, J. Qiao, J. Zhang, A review of high temperature co-electrolysis of H_2O and CO_2 to produce sustainable fuels using solid oxide electrolysis cells (SOECs): advanced materials and technology, Chem. Soc. Rev. 46 (2017) 1427-1463. https://doi.org/10.1039/C6CS00403B.

[3] C. Duan, R. Kee, H. Zhu, N. Sullivan, L. Zhu, L. Bian, D. Jennigns, R. O'Hayre, Highly efficient reversible protonic ceramic electrochemical cells for power generation and fuel production, Nat. Energy 4 (2019) 230-240. https://doi.org/10.1038/s41560-019-0333-2.

[4] H. Shimada, T. Yamaguchi, H. Kishimoto, H. Sumi, Y. Yamaguchi, K. Nomura, Y. Fujishiro, Nanocomposite electrodes for high current density over 3 A cm^{-2} in solid oxide electrolysis cells, Nat. Comm. 10 (2019) 5432. https://doi.org/10.1038/s41467-019-13426-5.

[5] H. Ding, W. Wu, C. Jiang, Y. Ding, W. Bian, B. Hu, P. Singh, C.J. Orme, L. Wang, Y. Zhang, D. Ding, Self-sustainable protonic ceramic electrochemical cells using a triple conducting electrode for hydrogen and power production, Nat. Comm. 11 (2019) 1907. https://doi.org/10.1038/s41467-020-15677-z.

[6] S. Wang, A. Inoishi, J.E. Gong, Y.W. Ju, H. Hagiwara, S. Ida, T. Ishihara, Ni–Fe bimetallic cathodes for intermediate temperature CO_2 electrolyzers using a $La_{0.9}Sr_{0.1}Ga_{0.8}Mg_{0.2}O_3$ electrolyte, J. Mater. Chem. A 1 (2013) 12455-12461. https://doi.org/10.1039/C3TA11863K.

[7] H. LV, L. Lin, X. Zhang, Y. Song, H. Matsumoto, C. Zeng, N. Ta, W. Liu, D. Gao, G. Wang, X. Bao, In situ investigation of reversible exsolution/dissolution of CoFe alloy nanoparticles in a Co-doped $Sr_2Fe_{1.5}Mo_{0.5}O_{6-\delta}$ cathode for CO_2 electrolysis, Adv. Mater. 32 (6) (2019) 1906193. https://doi.org/10.1002/adma.201906193.

[8] S.D. Ebbesen, S.H. Jensen, A. Hauch, M.B. Mogensen, High temperature electrolysis in alkaline cells, solid proton conducting cells, and solid oxide cells, Chem. Rev. 114 (2014) 10697-10734. https://doi.org/10.1021/cr5000865.

[9] L. Chen, F. Chen, C. Xia, Direct synthesis of methane from CO_2–H_2O co-electrolysis in tubular solid oxide electrolysis cells, Energy Environ. Sci. 7 (2014) 4018-4022. https://doi.org/10.1039/C4EE02786H.

[10] S.W. Kim, M. Park, H. Kim, K.J. Yoon, J.W. Son, J.H. Lee, B.K. Kim, J.H. Lee, J. Hong, In-situ nano-alloying Pd-Ni for economical control of syngas production from high-temperature thermo-electrochemical reduction of steam/CO_2, Appl. Catal. B: Environ. 200 (2017) 265-273. https://doi.org/10.1016/j.apcatb.2016.07.008.

[11] N. Duan, M. Gao, B. Hua, M. Li, B. Chi, J. Li, J.L. Luo, Exploring $Ni(Mn_{1/3}Cr_{2/3})_2O_4$ spinel-based electrodes for solid oxide cells, J. Mater. Chem. A, 8 (2020) 3988-3998. https://doi.org/10.1039/C9TA11878K.

[12] M. Trini, A. Hauch, S.D. Angelis, X. Tong, P.V. Hendriksen, M. Chen, Comparison of microstructural evolution of fuel electrodes in solid oxide fuel cells and electrolysis cells, J. Power Sources 450 (2020) 227599. https://doi.org/10.1016/j.jpowsour.2019.227599.

[13] B. Niu, C. Lu, W. Yi, S. Luo, X. Li, X. Zhong, X. Zhao, B. Xu, In-situ growth of nanoparticles-decorated double perovskite electrode materials for symmetrical solid oxide cells, Appl. Catal. B: Environ. 270 (2020) 118842. https://doi.org/10.1016/j.apcatb.2020.118842.

[14] X. Yue, J. T. S. Irvine, Alternative cathode material for CO_2 reduction by high temperature solid oxide electrolysis cells, J. Electrochem. Soc. 159 (2012) F442-F448. https://doi.org/10.1149/2.040208jes.

[15] X. Yue, J. T. S. Irvine, Impedance studies on LSCM/GDC cathode for high temperature CO_2 electrolysis, Electrochem. Solid-State Lett. 15 (2012) B31-B34. https://doi.org/10.1149/2.021203esl.

[16] C. Ruan, K. Xie, L. Yang, B. Ding, Y. Wu, Efficient carbon dioxide electrolysis in a symmetric solid oxide electrolyzer based on nanocatalyst-loaded chromate electrodes, Int. J. Hydrogen Energy 39 (2014) 10338-10348. https://doi.org/10.1016/j.ijhydene.2014.04.204.

[17] Q. Qin, C. Ruan, L. Ye, L. Gan, K. Xie, Efficient syngas production from methane reforming in solid oxide electrolyser with LSCM cathode loaded with Ni–Cu catalysts, J. Solid State Electrochem. 19 (2015) 3389-3399. https://doi.org/10.1007/s10008-015-2966-9.

[18] W. Qi, Y. Gan, D. Yin, Z. Li, G. Wu, K. Xie, Y. Wu, Remarkable chemical adsorption of manganese-doped titanate for direct carbon dioxide electrolysis, J. Mater. Chem. A 2 (2014) 6904-6915. https://doi.org/10.1039/C4TA00344F.

[19] S.P. Jiang, A review of wet impregnation-An alternative method for the fabrication of high performance and nano-structured electrodes of solid oxide fuel cells, Mater. Sci. Eng. A 418 (2006) 199-210. https://doi.org/10.1016/j.msea.2005.11.052.

[20] F. Bidrawn, G. Kim, G. Corre, J.T.S. Irvine, J.M. Vohs, R.J. Gorte, Efficient reduction of CO_2 in a solid oxide electrolyzer, Electrochem. Solid-State Lett. 11 (2018) B167-B170. https://doi.org/10.1149/1.2943664.

[21] X. Zhang, L. Ye, J. Ju, J. Li, W. Jiang, C. Tseng, K. Xie, Perovskite LSCM impregnated with vanadium pentoxide for high temperature carbon dioxide electrolysis, Electrochem. Acta 212 (2016) 32-40. https://doi.org/10.1016/j.electacta.2016.06.137.

[22] R. Xing, Y. Wang, Y. Zhu, S. Liu, C. Jin, Co-electrolysis of steam and CO_2 in a solid oxide electrolysis cell with $La_{0.75}Sr_{0.25}Cr_{0.5}Mn_{0.5}O_{3-\delta}$–Cu ceramic composite electrode, J. Power Sources 274 (2015) 260-264. https://doi.org/10.1016/j.jpowsour.2014.10.066.

[23] C. Zhu, L. Hou, S. Li, L. Gan, D. Xie, Efficient carbon dioxide electrolysis with metal nanoparticles loaded $La_{0.75}Sr_{0.25}Cr_{0.5}Mn_{0.5}O_{3-\delta}$ cathodes, J. Power Sources 363 (2017) 177-184. https://doi.org/10.1016/j.jpowsour.2017.07.070.

[24] Y. Zhou, L. Lin, Y. Song, X. Zhang, H. LV, Q. Liu, Z. Zhou, N. Ta, G. Wang, X. Bao, Pd single site-anchored perovskite cathode for CO_2 electrolysis in solid oxide electrolysis cells, Nano Energy 71 (2020) 104598. https://doi.org/10.1016/j.nanoen.2020.104598.

[25] W. Wang, L. Gan, J.P. Lemmon, F. Chen, J.T.S, Irvine, K. Xie, Enhanced carbon dioxide electrolysis at redox manipulated interfaces, Nat. Comm. 10 (2019) 1550. https://doi.org/10.1038/s41467-019-09568-1.

[26] Y. Zhou, Z. Zhou, Y. Song, X. Zhang, F. Guan, H. Lv, Q. Liu, S. Miao, G. Wang, X. Bao, Enhancing CO_2 electrolysis performance with vanadium-doped perovskite cathode in solid oxide electrolysis cell, Nano Energy 50 (2018) 43-51. https://doi.org/10.1016/j.nanoen.2018.04.054.

[27] X.J. Chen, K.A. Khor, S.H. Chan, L.G. Yu, Influence of microstructure on the ionic conductivity of yttria-stabilized zirconia electrolyte, Mat. Sci. Eng. A, 335 (2002) 246-252. https://doi.org/10.1016/S0921-5093(01)01935-9.

[28] J. Carneiro, E. Nikolla, Nanoengineering of solid oxide electrochemical cell technologies: An outlook. Nano Research, 12 (2019) 2081-2092. https://doi.org/10.1007/s12274-019-2375-y.

[29] J.S. Kim, N.L. Wieder, A.J. Abraham, M. Cargnello, P. Fornasiero, R.J. Gorte, J.M. Vohs, Highly active and thermally stable core-shell catalysts for solid oxide fuel cells, J. Electrochem. Soc 158, (2011) B596-B600. https://doi.org/10.1149/1.3571039.

[30] N. Kumari, P.K. Tiwari, M.A. Haider, S. Basu, Electrochemical Performance of Infiltrated Cu-GDC and Cu-PDC Cathode for CO2 Electrolysis in a Solid Oxide Cell, ECS Transactions, 78 (1) (2017) 3329-3337. https://doi.org/10.1149/07801.3329ecst.

[31] Y. Li, K. Xie, S. Chen, H. Li, Y. Zhang, Y. Wu, Efficient carbon dioxide electrolysis based on perovskite cathode enhanced with nickel nanocatalyst, Electrochim. Acta 153 (2015) 325-333. https://doi.org/10.1016/j.electacta.2014.11.151.

[32] W. Qi, Y. Gan, D. Yin, Z. Li, G. Wu, K. Xie, Y. Wu, Remarkable chemical adsorption of manganese-doped titanate for direct carbon dioxide electrolysis, J. Mater. Chem. A, 2 (2014 6904-6915. https://doi.org/10.1039/C4TA00344F

[33] X. Zhang, Y. Song, F. Cuan, Y. Zhou, H. Lv, Q. Liu, G. Wang, X. Bao, $(La_{0.75}Sr_{0.25})_{0.95}(Cr_{0.5}Mn_{0.5})O_{3-\delta}$-$Ce_{0.8}Gd_{0.2}O_{1.9}$ scaffolded composite cathode for high temperature CO_2 electroreduction in solid oxide electrolysis cell, J. Power Sources, 400 (2018) 104-113. https://doi.org/10.1016/j.jpowsour.2018.08.017.

[34] M.K. Khameneh, A. Babaei, Co-electrolysis of CO_2 and H_2O on $LaFe_{0.6}Co_{0.4}O_3$ promoted $La_{0.75}Sr_{0.25}Cr_{0.5}Mn_{0.5}O_3$/YSZ electrode in solid oxide electrolysis cell, Electrochim. Acta 299 (2019) 132-142. https://doi.org/10.1016/j.electacta.2018.12.136.

[35] T. Wang, J. Wang, L. Yu, Z. Ye, X. Hu, G.E. Marnellos, D. Dong, Effect of NiO/YSZ cathode support pore structure on CO_2 electrolysis via solid oxide electrolysis cells, J. Eur. Ceram. Soc. 38(15) (2018) 5051-5057. https://doi.org/10.1016/j.jeurceramsoc.2018.07.005.

[36] Y. Xie, J. Xiao, D. Liu, J. Liu, C. Yang, Electrolysis of carbon dioxide in a solid oxide electrolyzer with silver-gadolinium-doped ceria cathode, J. Electrochem. Soc. 162(4) (2015) F397-F402. https://doi.org/ 10.1149/2.0501504jes.

[37] S. Liu, Q. Liu, J. Luo, Highly Stable and efficient catalyst with in situ exsolved Fe-Ni alloy nanospheres socketed on an oxygen deficient perovskite for direct CO_2 electrolysis, Acs Catal. 6(9) (2016) 6219-6228. https://doi.org/10.1021/acscatal.6b01555.

[38] R.D. Green, C. Liu, S.B. Adler, Carbon dioxide reduction on gadolinia-doped ceria cathodes, Solid State Ionics, 179(17-18) (2008) 647-660. https://doi.org/10.1016/j.ssi.2008.04.024.

[39] Y. Matsuzaki, I. Yasuda, Electrochemical oxidation of H_2 and CO in a H_2-H_2O-CO-CO_2 system at the interface of a Ni-YSZ cermet electrode and YSZ electrolyte, J. Electrochem. Soc. 147(5) (2000) 1630-1635. https://doi.org/10.1149/1.1393409.

[40] Y. Luo, W. Li, Y. Shi, N. Cai, Mechanism for reversible CO/CO_2 electrochemical conversion on a patterned nickel electrode, J. Power Sources 366 (2017) 93-104. https://doi.org/10.1016/j.jpowsour.2017.09.019.

[41] J. Qiao, Y Liu, J. Zhang, Electrochemical Reduction of Carbon Dioxide Fundamentals and Technologies, 1st ed., Routledge, 2019.

[42] V.M. Janardhanan, O. Deutschmann, Modeling of solid-oxide fuel cells, Z. Phys. Chem. 221 (2007) 443-478. https://doi.org/10.1524/zpch.2007.221.4.443.

[43] J. Lu, C. Zhu, C. Pan, W. Lin, J.P. Lemmon, F. Chen, C. Li, K. Xie, Highly efficient electrochemical reforming of CH_4/CO_2 in a solid oxide electrolyser, Sci. Adv. 4 (2018) eaar5100. https://doi.org/10.1126/sciadv.aar5100.

[44] M. Guo, J. Lu, Y. Wu, Y. Wang, M. Luo, UV and visible Raman studies of oxygen vacancies in rare-earth-doped ceria. Langmuir 27 (2011) 3872-3877. https://doi.org/10.1021/la200292f.

[45] W. Miśta, M. A. Małecka, L. Kępiński, Redox behavior of nanocrystalline $Ce_{1-x}Lu_xO_{2-x/2}$ mixed oxide obtained by microemulsion method, Appl. Catal. A: Gen. 368(1-2) (2009) 71-78. https://doi.org/10.1016/j.apcata.2009.08.011.

[46] T. Mori, R. Buchanan, D.R. Ou, R. Ye, T. Kobayashi, J.D. Kim, J. Zlu, J. Drennan, Design of nanostructured ceria-based solid electrolytes for development of IT-SOFC, J. Solid State Electrochem. 12 (2008) 841-849. https://doi.org/10.1007/s10008-007-0444-8.

[47] M. Coduri, M. Scavini, M. Pani, M. M. Carnasciali, H. Klein, C. Artini, From nano to microcrystals: effects of different synthetic pathways on the defect architecture in heavily Gd-doped ceria, Phys. Chem. Chem. Phys. 19 (2017) 11612-11630. https://doi.org/10.1039/C6CP08173H.

[48] G. Tao, K.R. Sridhar, C. L. Chan, Study of carbon dioxide electrolysis at electrode/electrolyte interface: Part I. Pt/YSZ interface, Solid State Ionics 175 (2004) 615-619. https://doi.org/10.1016/j.ssi.2004.01.077.

[49] A.B. Hungría, A. Martínez-Arias, M. Fernández-García, A. Iglesias-Juez, A. Guerrero-Ruiz, J.J. Calvino, J.C. Conesa, J. Soria, Structural, morphological, and oxygen handling properties of nanosized cerium−terbium mixed oxides prepared by microemulsion, Chem. Mater. 15(22) (2003) 4309-4316. https://doi.org/10.1021/cm031028n.

[50] S. Rossignol, F. Gérard, D. Mesnard, C. Kappenstein, D. Duprez, Structural changes of Ce-Pr-O oxides in hydrogen: a study by in situ X-ray diffraction and Raman spectroscopy, *J. Mater. Chem.* 13 (2003) 3017-3020. https://doi.org/10.1039/B306726B.

[51] R.D. Green, C. Liu, and S.B. Adler, Carbon dioxide reduction on gadolinia-doped ceria cathodes, Solid State Ionics 179 (2008) 647-660. https://doi.org/10.1016/j.ssi.2008.04.024.

[52] X. Yue, J.T.S. Irvine, Modification of LSCM–GDC cathodes to enhance performance for high temperature CO_2 electrolysis using solid oxide electrolysis cells (SOECs), J. Mater. Chem. A5 (2017) 7081-7090. https://doi.org/10.1039/C6TA09421J.

Table. 1 Current density at various voltage for CO_2 electrolysis using different composite electrodes that are operated from 1073 to 1123 K, respectively.

Cathode electrode	Electrolyte	Anode electrode	Working condition	Current density (mA cm^{-2})	Ref.
Cu@PDC	YSZ	LSM	CO_2/H_2 mixture (56:44 vol.%) at 1023 K	69 at 2.0 V	[30]
LSTMN@YSZ	YSZ	LSM-YSZ	CO_2 at 1073 K	25 at 1.2 V	[31]
LSTM@SDC	YSZ	LSM-SDC	CO_2 at 1073 K	250 at 2.0 V	[32]
LSCM-GDC@YSZ	YSZ	LSM-ScSZ	CO_2 at 1073 K	278 at 1.6 V	[33]
LFC-LSCM@YSZ	YSZ	-	CO_2/H_2O (9:20 vol.%) at 1123 K	300 at 1.5 V	[34]
Ni-YSZ	YSZ	LSCF-GDC	CO_2/H_2O (70:30 vol.%) at 1073 K	15 at 1.2 V	[35]
Pd-GDC@LSCM	YSZ	LSCF-YSZ	CO_2-CO mixture (50:50 vol.%) at 1123 K	346 at 1.5 V	This work

LSTMN= $(La_{0.2}Sr_{0.8})_{0.9}(Ti_{0.9}Mn_{0.1})_{0.9}$; $Ni_{0.1}O_{3-\delta}$, LSM= $La_{0.8}Sr_{0.2}MnO_{3+\delta}$, SDC= $Ce_{0.8}Sm_{0.2}O_{2-\delta}$, LSTM= $La_{0.2}Sr_{0.8}Ti_{0.9}Mn_{0.1}O_{3-\delta}$, LSCM= $La_{0.75}Sr_{0.25}Cr_{0.5}Mn_{0.5}O_{3-\delta}$, LFC: $LaFe_{0.6}Co_{0.4}O_3$, LSCF: $La_{0.6}Sr_{0.4}Co_{0.2}Fe_{0.8}O_3$,

Table. 2 Area specific resistance (ASR) data obtained from equivalent-circuit analysis through the EIS of the Pd-GDC@LSCM cathode under OCV conditions and at 0.5 V using different working temperatures under a CO_2/CO (50:50 vol.%) atmosphere for CO_2 electrolysis on the SOECs.

Temperature K	R_s (Ω cm^2)		R_{p1} (Ω cm^2)		R_{p2} (Ω cm^2)		R_p (Ω cm^2)
	OCV	0.5 V	OCV	0.5 V	OCV	0.5 V	OCV
1123	0.867	0.881	0.155	0.177	0.650	0.384	0.804
1073	0.880	0.805	0.070	0.085	0.919	0.441	0.989
1023	1.138	1.050	0.289	0.274	1.359	0.532	1.648

Table. 3 Summary of R_p values from the different processes for fabrication of a GDC-LSCM cathode for the CO electrolyte in CO_2/CO systems

CO_2/CO ratio	R_p at OCV (Ω cm^2)			
	GDC-LSCM (Screen-printing, 1573 K)	GDC-LSCM (Screen-printing, 1473 K)	Pd-GDC@LSCM (In this work)	
50/50	0.84 [14, 15]	0.80 [35]	0.80	0.56
Operating Temperature	1173 K at OCV	1173 K at OCV	1123 K at OCV	1123 K at 0.5 V

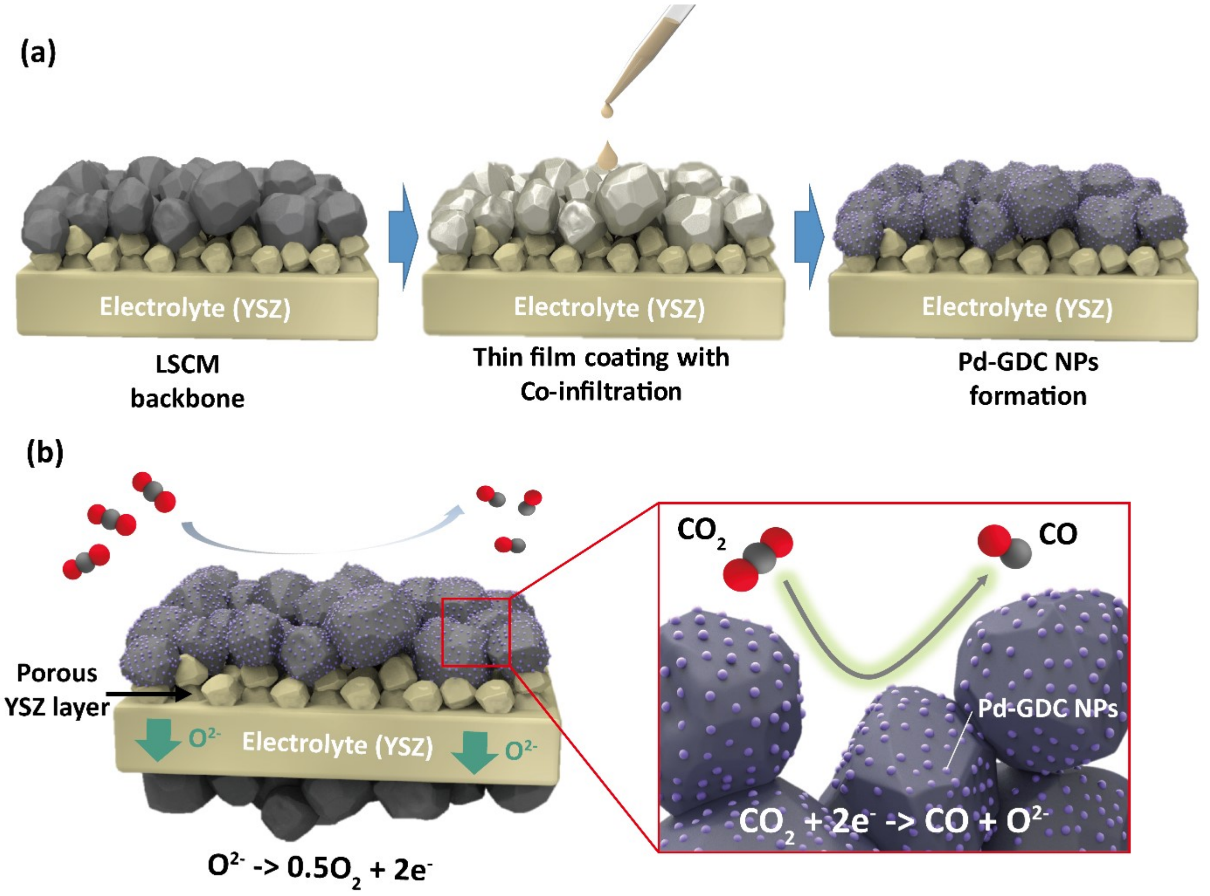

Figure 1. (a) Schematic of the infiltration process of the Pd-GDC@LSCM. The porous electrode backbone is prepared and then the backbone is fired at high temperature to ensure excellent bonding with the electrolyte, excellent connectivity for effective conduction of electron and oxygen ion, and good structural stability of the electrode under operation conditions. A liquid solution containing the stoichiometric metal salt precursors for Pd-GDC is introduced into a pre-sintered backbone. After subsequent thermal treatment, Pd-GDC nanoparticles are formed on the surface of the backbone. (b) Schematic representation of the electrochemical CO_2 electrolysis process in a SOEC. CO_2 electrolysis is performed on the cathode, whereas the oxygen evolution reaction of O_2 is carried out on the anode.

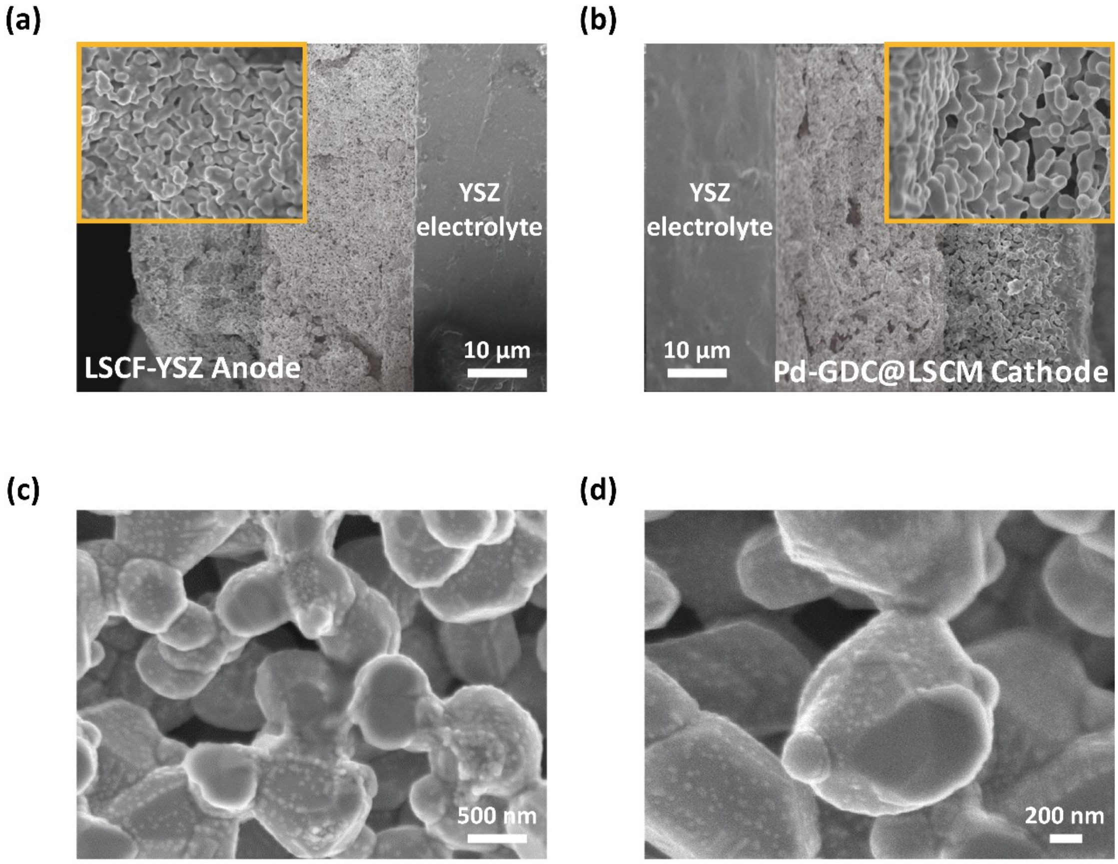

Figure 2. Cross-sectional SEM images of (b) the YSZ-supported LSCF anode, and (c) the Pd-GDC@LSCM cathode. Insets show enlarged cross-sectional SEM images. Incorporation of the porous YSZ layers (brighter parts in (b) and (c)) between the electrolyte and the LSCM layer avoids deterioration of the cathode/electrolyte interface. (d) SEM image of the infiltrated Pd-GDC particles, and (e) enlarged SEM image of the infiltrated Pd-GDC particles. The Pd-GDC nanoparticles anchor on the surface of LSCM. The nanoparticles display a high dispersion, with an average of 50–70 nm, which should deliver highly active exsolved interfaces for CO_2 electrolysis. A LSCM:CGO:Pd = 90:10:1 wt.% weight percent ratio was maintained.

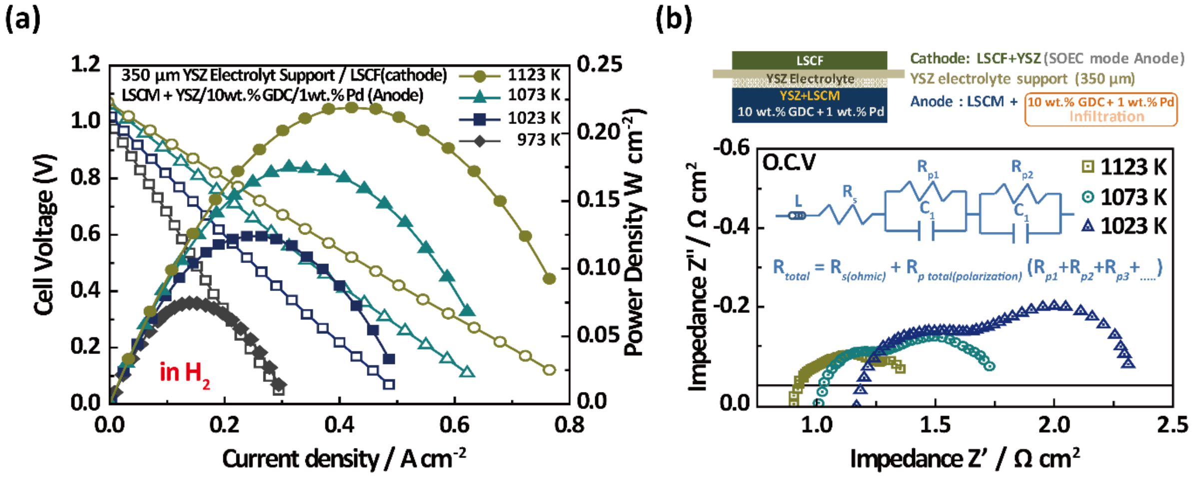

Figure 3. (a) Cell voltage and power density versus current density for the SOFC mode operation with a Pd-GDC@LSCM anode. (b) Configuration of the fabricated solid oxide unit single cell for the SOFC/SOEC mode and impedance spectra for the SOFC mode at OCV conditions at a range of temperatures.

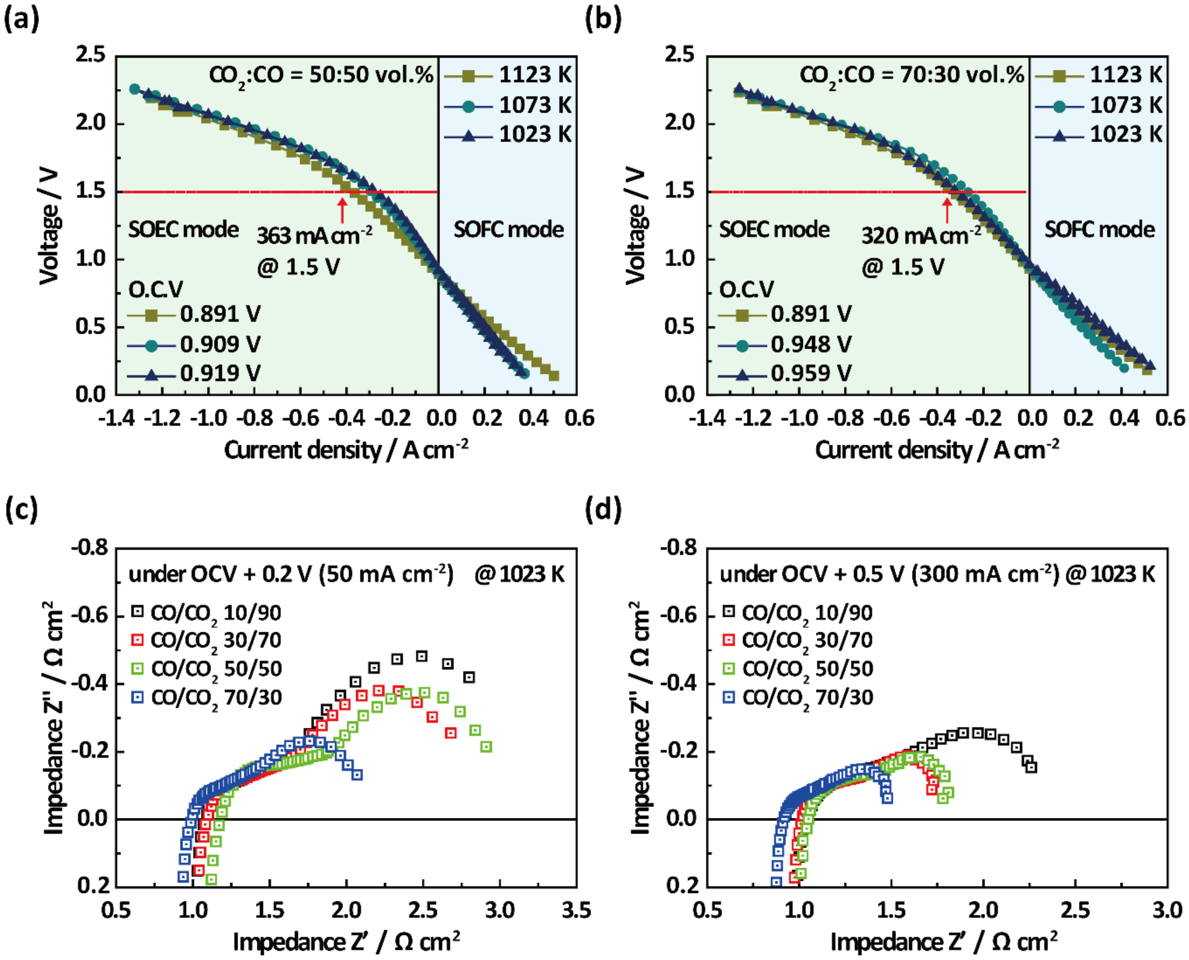

Figure 4. I-V curves of the SOEC containing the Pd-GDC co-infiltrated LSCM cathode operating under (a) CO_2-CO (50:50 vol.%) and (b) CO_2-CO (70:30 vol.%) conditions at different working temperatures ranging from 1023 to 1123 K. Impedance spectra of the SOEC for the Pd-GSC@LSCM cathode under (c) 0.2 V (50 mA cm^{-2}) and (d) 0.5 V (300 mA cm^{-2}) under different atmospheres at 1023 K (black: CO/CO_2 10/90, red: CO/CO_2 30/70, green: CO/CO_2 50:50, and blue: CO/CO_2 70:30).

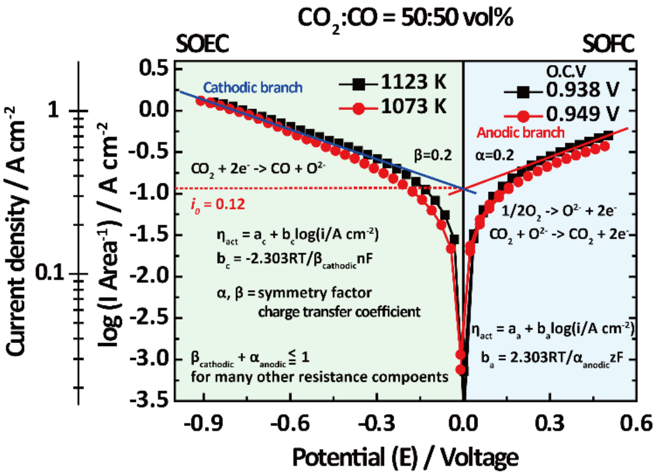

Figure 5. Current density as a function of the electrode potential including the corresponding overpotential Tafel slope fit to the Bulter-Volmer equation; for the Pd-GDC co-infiltrated LSCM cathode operating under CO_2-CO (50:50 vol.%) conditions with working temperatures of 1073 and 1123 K. Tafel-like behavior is shown for the cell overpotential vs. the logarithm of current density.

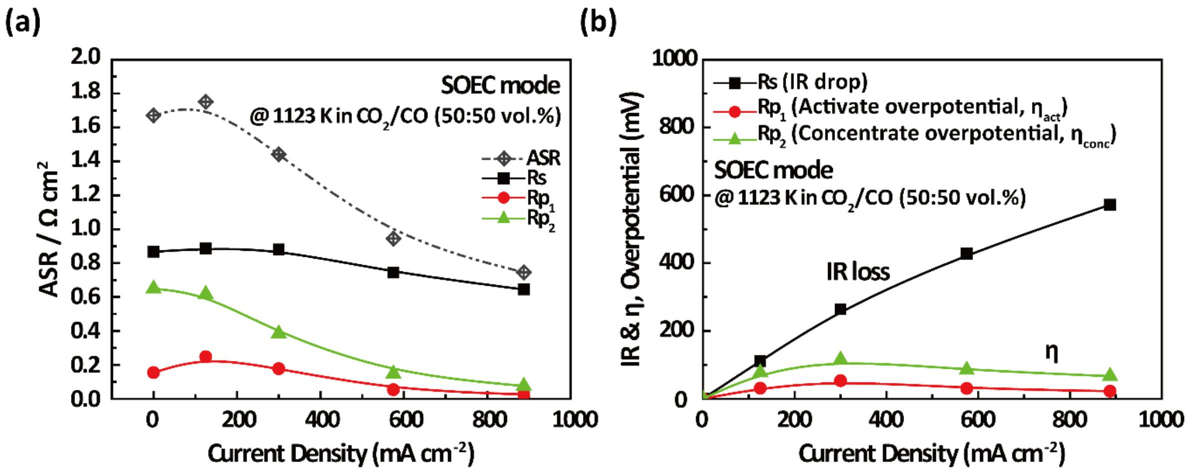

Figure 6. (a) ASR and (b) polarization curves from the equivalent-circuit analysis of the EIS of the Pd-GDC co-infiltrated LSCM cathode under OCV conditions at 1123 K under CO_2/CO (50:50 vol.%) for CO_2 electrolysis using the SOEC.

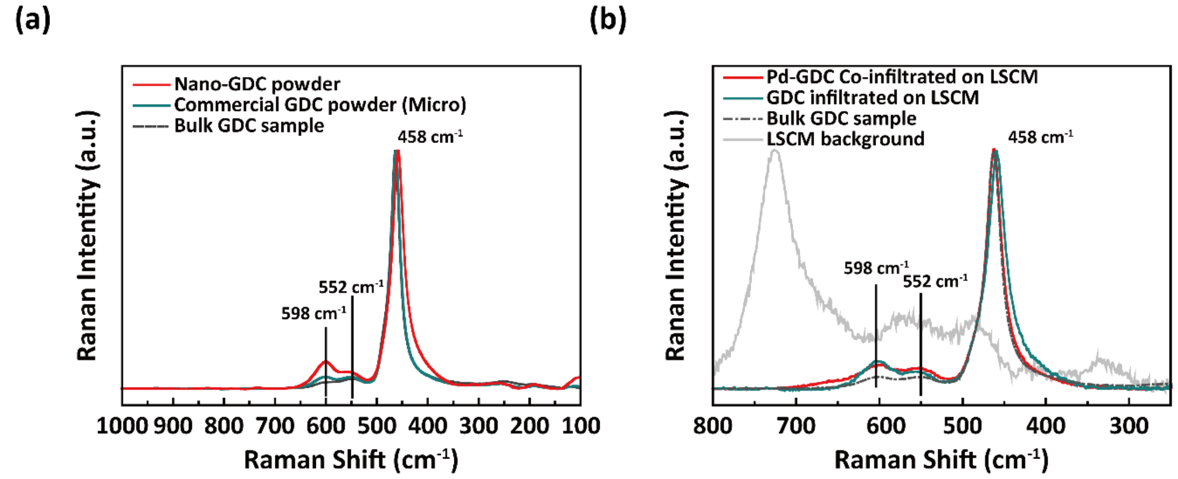

Figure 7. Raman spectra of (a) GDC bulk sample, Commercial GDC powder (FCM Co.Ltd., USA) and Nano-GDC powder, which was synthesized from infiltration nitrate solution,; (b) Pd-GDC co-infiltrated LSCM cathode, GDC infiltrated LSCM cathode, LSCM porous scaffolds cathode at 458, 552 and 598 cm^{-1} excitation laser line.

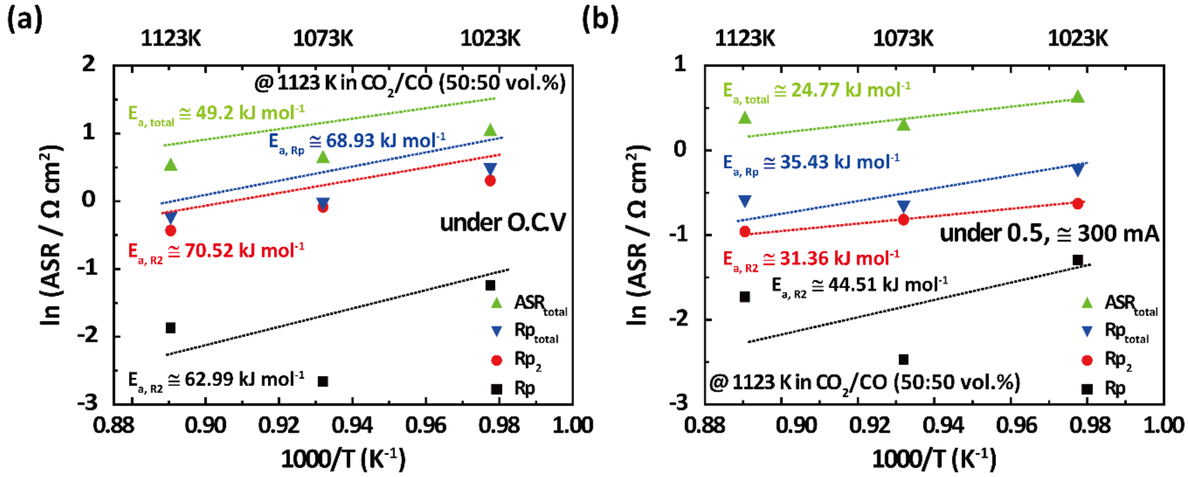

Figure 8. Arrhenius plot of the polarization resistance of the PD-GDC@LSCM cathode at (a) OCV conditions and (b) 0.5 V (loading ~300 mV) over a range of operating temperatures under CO_2/CO (50:50 vol.%) conditions for CO_2 electrolysis using the SOEC.

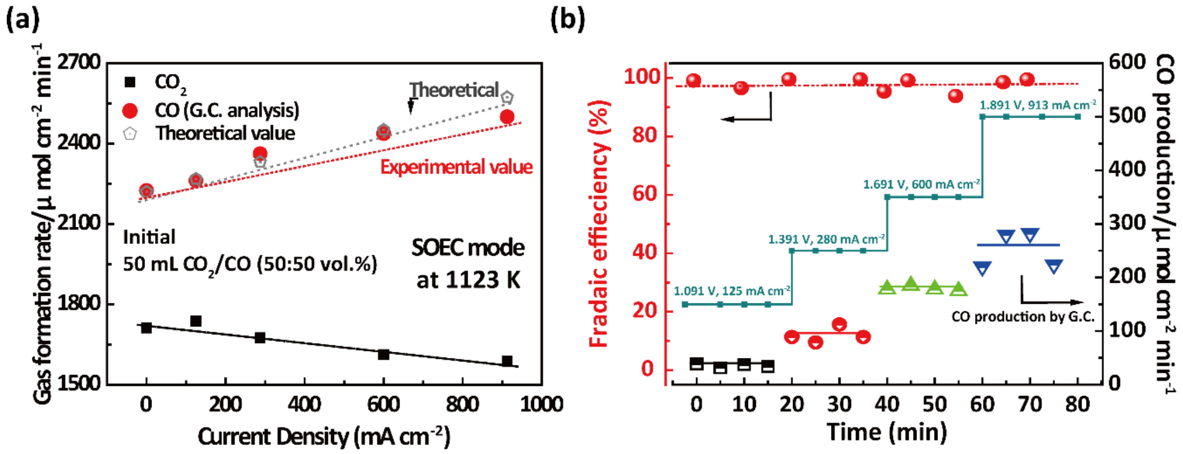

Figure 9. The gas formation rate of the Pd-GDC@LSCM/YSZ/LSCF SOC cell during CO_2 electrolysis at 1123 K, measured by G.C. ; (a) Gas formation from CO_2 reduction as a function of applying constant current and (b) CO production and Faradaic efficiency for electrocatalytic CO_2 reduction at different voltages and operating temperature of 1123 K.

Graphic abstract